Applied Thermal Engineering 279 (2025) 127541

Contents lists available at ScienceDirect

Applied Thermal Engineering

journal homepage: www.elsevier.com/locate/apthermeng

Research Paper

# ReSONS: A novel regional split optimization method with numerical simulation for condensers

Ruihan Zhang [a], Yuxin Wu [a,*], Xiongshi Wang [a], Shoubao Dai [b,**], Tengteng Zhan [b], Guihua Zhang [a], Junfu Lyu [a]

[a] Department of Energy and Power Engineering, Key Laboratory for Thermal Science and Power Engineering of Ministry of Education, Tsinghua University, Beijing 100084, China

[b] State Key Laboratory for Marine Thermal Energy and Power, Harbin Ship Boiler Turbine Research Institute, Harbin 150078, China

ARTICLE INFO

*Keywords:*
Shell-and-tube condenser
Multiphase CFD
Particle swarm optimization
Regional split
Tube bundle design

ABSTRACT

In this study, a novel Regional Split Optimization with Numerical Simulation (ReSONS) method is proposed to integrate CFD simulations with automated optimization for shell-and-tube condensers. Conventional optimization methods typically use global design parameters and simplified models, limiting their ability to leverage detailed CFD flow and heat transfer information. To overcome this limitation, the ReSONS method splits the tube bundle region into multiple subregions, each assigned a porosity variable as localized design parameter representing tube density to be optimized. The performance of each design is evaluated through CFD simulations, which allows for finer designs and better performance. A two-dimensional multiphase CFD solver was developed and validated for shell-and-tube condensers, then coupled with the Particle Swarm Optimization (PSO) algorithm to search for optimal porosity distributions. The pressure drop and condensation rate are considered in the objective function to enhance overall performance. Compared to conventional methods, the ReSONS method reduced pressure drop and the uncondensed ratio by 25% and 63%, respectively, for an experimental condenser case. This improvement is attributed to the enhanced design flexibility and expanded search space for tube bundle parameters, surpassing the limitations of global optimization strategy. Besides, the resulting design showed a pattern resembling a steam channel near the inlet, which is consistent with engineering expectations. The results indicate that the regional split optimization method can effectively incorporate local characteristics into the design process, offering a new approach to CFD coupled localized tube bundle optimization.

## 1. Introduction

The condenser is a critical auxiliary equipment in steam power systems, functioning as the cold sink that directly influences the system's thermal efficiency and operational reliability. Among the various types, shell-and-tube condensers are widely utilized in power generation, waste heat recovery, and other industrial applications. This type of condenser consists of a pressure vessel (shell) housing a densely arranged bundle of heat exchange tubes. Typically, cooling water flows inside the tubes, while steam enters the shell side and condenses on the outer surface of the tubes. The condensate collects in the hotwell at the bottom of the condenser and is discharged out. The internal pressure of the condenser corresponds to the saturation pressure of steam at approximately 30 °C, which is significantly lower than atmospheric pressure and it helps to establish a vacuum at the turbine outlet. In addition to steam and condensed water, the condenser often contains a certain amount of non-condensable gas.

With technological advancements, increasing attention is being directed towards improving condenser performance. Achieving compact and efficient designs for large-scale condensers relies on the optimization of design parameters, which requires an accurate evaluation of internal flow and heat transfer characteristics. While experimental methods provide the most reliable data, both full-scale and scaled-down experiments are costly and time-consuming, making them impractical for extensive parameter studies during the early design stages. Traditional condenser design methods often rely on analytical models derived from theoretical principles and empirical correlations based on extensive experimental data. However, these models are often limited in their ability to reveal detailed internal flow and heat transfer behaviors,

* Corresponding author.
** Corresponding author at: Harbin Ship Boiler Turbine Research Institute, Harbin, China.
*E-mail addresses:* zhang-rh23@mails.tsinghua.edu.cn (R. Zhang), wuyx09@tsinghua.edu.cn (Y. Wu), 124918232@qq.com (S. Dai).

https://doi.org/10.1016/j.applthermaleng.2025.127541
Received 11 April 2025; Received in revised form 11 July 2025; Accepted 12 July 2025
Available online 13 July 2025

**Nomenclature**

*English symbols*

| | |
|---|---|
| $D_e$ | Diffusivity |
| $D_d$ | Droplet diameter |
| $D_i$ | Tube inner diameter |
| $D_o$ | Tube outer diameter |
| $L_{lg}$ | Latent heat of condensation |
| Len | Condenser length |
| $\dot{M}_{cw}$ | Cooling water flow rate |
| Nu | Nusselt number |
| $P_t$ | Tube pitch |
| $Pr$ | Prandtl number |
| Re | Renold number |
| $R_{tot}$ | Total thermal resistance |
| $T$ | Temperature |
| $U_m$ | Physical velocity magnitude |
| $V_c$ | Control volume |
| $Y$ | Mass fraction |
| $c_p$ | Specific heat capacity at constant pressure |
| $\mathbf{g}_k^t$ | Global best position |
| $\dot{m}$ | Condensation rate |
| $n_t$ | Number of tubes in control volume |
| $p$ | Pressure |
| $\Delta p_s$ | Steam pressure drop |
| $\mathbf{p}_k^t$ | Personal best position |
| $u_i$ | Physical velocity component |
| $\mathbf{v}_k^t$ | Particle velocity |
| $x_i$ | Coordinate component |
| $\mathbf{x}_k^t$ | Particle position |

*Greek symbols*

| | |
|---|---|
| $\alpha$ | Volume fraction |
| $\beta$ | Local porosity |
| $\beta_t$ | Porosity in the tubular region |
| $\lambda$ | Thermal conductivity |
| $\rho$ | Density |
| $\mu$ | Dynamic viscosity |
| $\omega^t$ | Inertial weight |

*Subscript*

| | |
|---|---|
| a | Air |
| c | Condensate |
| cw | Cooling water |
| g | Gas phase |
| i | Free index (Direction) |
| j | Dummy index |
| l | Liquid phase |
| p | Phase (gas or liquid) |
| s | Saturated steam |
| t | Tube/Iteration step (superscript) |
| k | Particle index |

which constrains the development of advanced and refined design solutions.

Computational fluid dynamics (CFD) has emerged as a key tool for condenser design by providing detailed insights into internal flow behavior. Compared to analytical models, CFD simulations offer spatial distributions of flow and heat transfer variables, enabling comprehensive performance evaluations that encompass the analysis of both global metrics and localized phenomena. Moreover, CFD enables the analysis of complex design variations, such as tube arrangement and spacing, which are difficult to model accurately using analytical methods.

Given the complexity of the flow field inside a condenser, which involves two-phase flow with phase change, turbulence, and multi-component, developing a numerical model capable of accurately predicting these phenomena is challenging. Based on the porous media model introduced by Patankar and Spalding [1], a series of works have been done by Zhang [2–4], Hu [5,6] and Mirzabeygi [7,8] et al. on developing condenser numerical models. Among which the discussion of model dimensionality is included. Due to the presence of baffles that restrict axial flow, two-dimensional simulations are commonly employed [2]. When axial variations are non-negligible, quasi-three-dimensional models [3,4] can be adopted to strike a balance between computational efficiency and accuracy. Full three-dimensional models [7], while providing highest fidelity, are generally reserved for specific cases due to their high computational cost.

To achieve improved performance, numerous studies have employed CFD methods to investigate the flow and heat transfer characteristics of shell-and-tube heat exchangers. Guo et al. [9] performed two-dimensional, single-phase simulations using Fluent to compare condensers with equilateral triangular and isosceles triangular tube bundle arrangements. The results showed that the equilateral triangular arrangement had the advantage of lower pressure drop, whereas the isosceles triangular arrangement achieved a higher heat transfer coefficient. Zeng et al. [10,11] examined condenser performance for three different tube bundle configurations using two-dimensional, single-phase models, with a focus on flow field characteristics and mechanical energy losses. They also predicted the performance of newly designed tube bundles. Kumar et al. [12] carried out extensive three-dimensional simulations to study the effects of tube and fin dimensions on the performance of air-cooled condensers and employed the Taguchi method to optimize design parameters. Abeykoon [13] compared the effects of baffle count, baffle cut ratio, and tube count on heat exchanger performance under consistent thermal loads. Their results demonstrated good consistency between CFD simulations and theoretical calculations. In addition to these studies, further research has explored the influence of heat exchanger dimensions [14] and operating conditions [15,16], highlighting the versatility of CFD in evaluating and optimizing various design configurations.

Many existing studies rely on manually adjusting parameters to compare the performance of different design configurations. This approach limits the exploration to a small set of predefined cases. To efficiently search a broader design space beyond empirical experience, some researchers have adopted optimization algorithms for automated parameter tuning. Among these, evolutionary algorithms are particularly favored in engineering applications due to their tolerance of models which are hard to mathematically analyze. Genetic algorithms (GA) and Particle Swarm Optimization (PSO) have been extensively applied to heat exchanger optimization problems, demonstrating promising results [17–22]. Other methods, such as simulated annealing [23] and harmony search [24], have also found applications in this field. Wang et al. [17] were among the first to report the application of GA algorithm to optimize heat exchangers. Their study significantly reduced the equipment's weight and enhanced compactness without increasing pressure drop, showcasing the potential of GA in heat exchanger optimization. Patel et al. [18] used PSO to optimize the structural parameters of heat exchangers with total cost as the objective, achieving lower costs across three cases compared to GA. Fettaka et al. [19] performed multi-objective optimization using GA to minimize heat transfer area and pressure drop, and found that discrete and continuous design variables yielded comparable results. Daneshparvar et al. [25] combined CFD simulations with GA for multi-objective optimization of

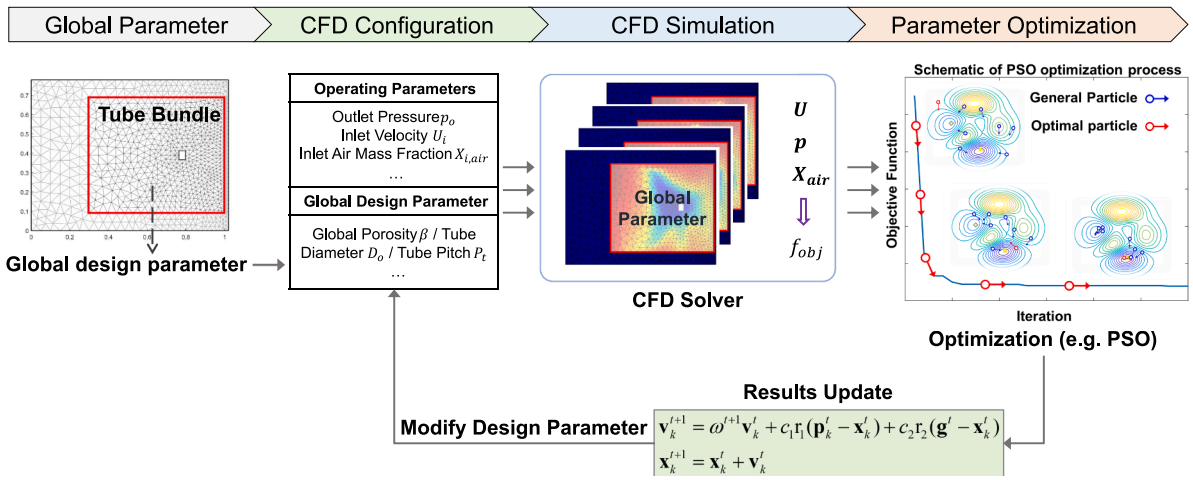


**Fig. 1.** Schematic of conventional global optimization of condenser tube bundle. Using a global design parameter to describe a uniform tube arrangement.

shell-and-tube condensers, obtaining Pareto fronts for pressure drop and heat transfer coefficients under helical baffle configurations. While GA remains a popular choice, some researchers argue that PSO achieves better results in heat exchanger optimization [20,26]. Depending on the design goals, optimization objectives for heat exchangers may include performance metrics [21,22,25,27] (e.g., pressure drop, entropy generation rate), geometric dimensions [17,23] (e.g., weight, compactness), cost factors [18] (e.g., construction and operating costs), or combinations of multiple objectives [19–21]. For a comprehensive review of evolutionary algorithms applied to shell-and-tube heat exchanger optimization, readers may refer to the work by Saldanha [28].

Currently, most automated heat exchanger optimization studies rely on the Bell-Delaware method [29] to evaluate the shell-side heat transfer coefficient and pressure drop. While CFD simulations provide richer information compared to traditional methods, they are primarily used to evaluate a limited number of design schemes. Only a few studies have attempted to combine CFD simulations with optimization algorithms [12,25,30].

A key challenge in utilizing CFD data for tube bundle optimization lies in effectively incorporating the complex physical information into the design process. Fig. 1 illustrates the design strategy that most CFD coupled optimization studies adopt currently, where a uniform tube pitch and tube diameter are typically applied across the entire tube bundle, and these global design parameters are optimized through an iterative process. However, this global optimization strategy leaves limited space for design variations and usually fails to fully leverage the detailed CFD results for more refined designs. Tube bundle arrangement has a pronounced influence on the characteristics of fluid and heat transfer inside the condenser, which should be carefully considered in the optimization process. Despite this, there still lacks an effective optimization method that fully accounts for this interaction. To enhance the utilization of CFD data in tube bundle optimization, a straightforward approach would be to assign independent design variables to each computational cell in the CFD mesh. While this allows maximum design flexibility, it results in a high-dimensional optimization problem that is computationally prohibitive and impractical for engineering use. Therefore, a trade-off must be achieved between design flexibility and computational feasibility when utilizing CFD results for tube bundle optimization.

To address this limitation, a novel Regional Split Optimization with Numerical Simulation (ReSONS) method was proposed. In this method, the tube bundle is divided into multiple subregions, each characterized by an independent porosity value that serves as the local design variable. These porosity values are embedded directly into the CFD configuration and optimized using a PSO algorithm. This coupling allows the CFD-derived flow and heat transfer results to influence localized tube

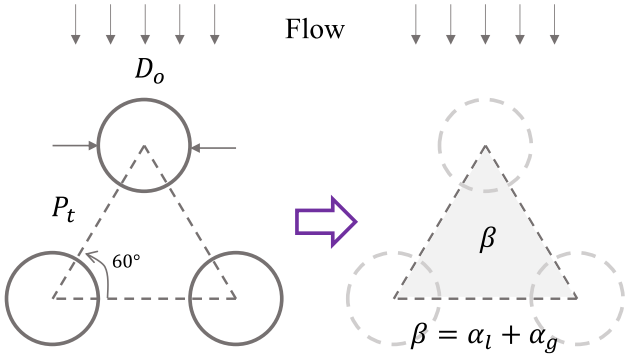


**Fig. 2.** Schematic of the relationship between porosity and tube parameters for triangular layout.

bundle optimization. Compared with global optimization method, ReSONS allows for regional design variation without incurring excessive optimization dimensionality. According to the authors' knowledge, it's the first time to combine the CFD flow characteristics with the optimization algorithms through a regionally split design strategy, which introduces a novel design perspective for CFD coupled tube bundle optimization.

This paper is organized as follows: Section 2 introduces the framework of the ReSONS method, the multiphase condenser numerical model and the Particle Swarm Optimization (PSO) algorithm. Section 3 presents the validation of the proposed method using an experimental condenser and an industrial condenser, including the problem description and a discussion of the results. Finally, Section 4 concludes the study with a summary of key findings.

## 2. Methodology

### 2.1. Porous media model

The flow paths for vapor and liquid phases within a shell-and-tube condenser are highly complex due to the dense arrangement of tube bundles in the condensation region. Directly discretizing the actual inter-tube flow area incurs significant efforts, making it time consuming and high-cost to simulate various tube bundle configurations using CFD. Consequently, many reported condenser CFD simulations adopt the porous media model [1] to simplify the representation of the tube bank. This modeling approach has been validated against experimental data, confirming its reliability and effectiveness [8].

In this approach, the density of the tube arrangement is reflected by

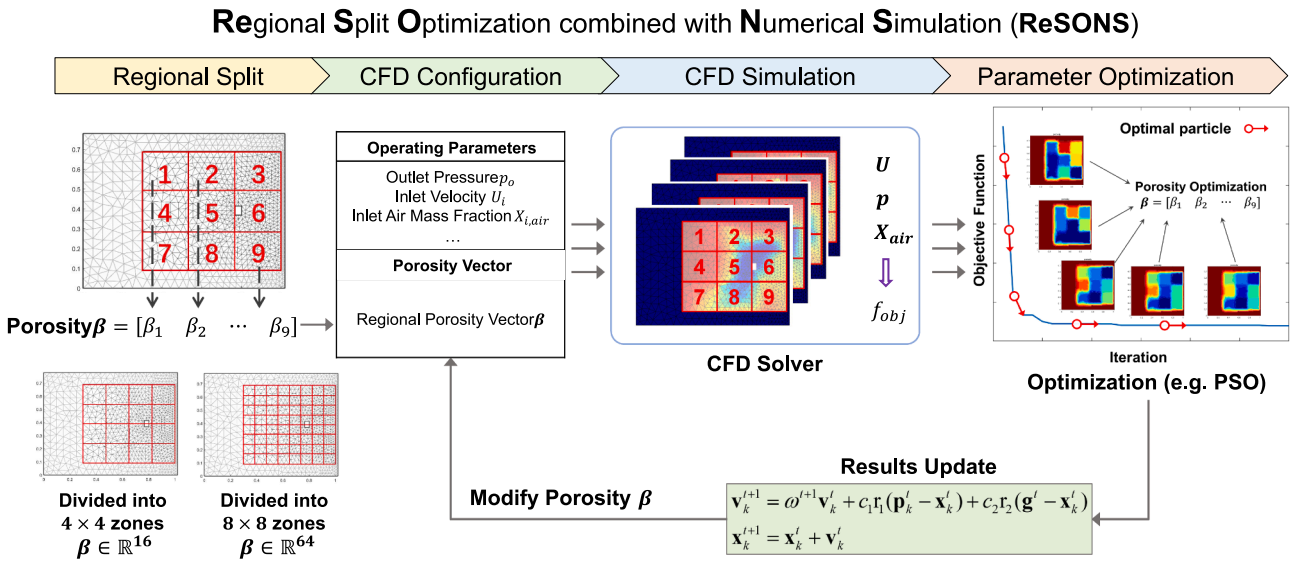


**Fig. 3.** Schematic of ReSONS framework for condenser tube bundle optimization. Local design parameters assigned to each subregion of the tube bundle.

the porosity $\beta$ of the medium, which is defined as the ratio of the volume occupied by fluid to the total volume within a computational cell. For the triangular layout (Fig. 2), porosity depends on the tube outer diameter $D_o$ and tube pitch $P_t$, and is calculated by the following equation:

$$\beta = 1 - \frac{\pi}{2\sqrt{3}} \left(\frac{D_o}{P_t}\right)^2 \tag{1}$$

In regions without tubes, $\beta = 1$. In the proposed CFD coupled optimization framework, porosity serves as a bridge between the numerical simulation and the optimization algorithm. For clarity and convenience, $\beta$ was directly used as the optimization parameter in this study.

### 2.2. Regional split optimization with numerical simulation (ReSONS) framework

To utilize CFD simulation results for design optimization, the CFD solver has to be integrated into the optimization iteration loop. Currently, some advanced large-scale industrial condensers adopt different design strategies for different regions. Inspired by this industrial practice, we proposed the regional split optimization method. The framework of the ReSONS method is illustrate in Fig. 3. The optimization process begins with splitting the tube bundle region into multiple subregions with independent porosity variables. The division of subregions can reflect similar flow and heat characteristics or just simple rectangular blocks. The randomly initialized porosity vector $\beta$ containing each subregion to be optimized is incorporated into the CFD configuration and updated iteratively during optimization. In this work, the update of porosities is realized through PSO algorithm, with each particle represents a different porosity vector in the design space. The CFD solver computes the spatial distribution of key physical quantities by solving the governing equations and evaluates the corresponding performance metrics for each particle. After all the particles are solved, the optimization algorithm assesses their effectiveness based on an objective function formulated from the performance metrics. Through minimizing the objective function, the optimizer then generates a new set of porosity vectors, after the CFD configurations are updated with the new porosity vectors, simulations are performed again to evaluate these new designs. This iterative process continues until either the maximum number of iterations is reached or the objective function converges to a predefined threshold.

This regional splitting strategy significantly reduces the total number of design variables compared to assigning them to individual mesh cells, while also aligning better with practical engineering and manufacturing constraints. For instance, if the bundle region is divided into 9 subregions, the optimization variable is a 9-dimensional porosity vector, which not only increases the design flexibility but also maintains a manageable optimization space dimensionality.

The optimized porosity distribution provides guidance on the regional tube density. For the single pass condensers, the porosity change can be achieved by changing the tube pitch within a subregion, as the subregions are relatively large, such adjustment is feasible. And for multi-pass condensers, the porosity values in different regions are not fully independent. In the optimization process, the porosity in the second pass subregions can be constrained to match that of the first pass, and regional porosity optimization is then applied only to the first pass domain.

### 2.3. Multiphase numerical model

#### 2.3.1. Governing equations

To enable more accurate performance predictions, a two-dimensional multiphase numerical model is developed to simulate the flow behavior of both gas and liquid phases within the condenser. The model is developed based on the following assumptions:

1. The gas phase is treated as a mixture of steam and air with constant viscosity, where air is modeled as a pure gas;
2. The steam–air mixture follows the behavior of a perfect gas;
3. Both steam and condensate are assumed to be saturated, and the re-evaporation of condensate is neglected;
4. The liquid condensate is modeled as droplets with diameter of 1 mm [31] (diffusion of the condensate is neglected);
5. Gas and liquid phases share the same pressure field;
6. The turbulent diffusivity is equal to the turbulent viscosity ($Sc = 1$);
7. Due to the high tube bundle density, the frictional coefficient is much higher than turbulent viscosity $\mu_t$, so a constant $\mu_t$ is adopted in this simulation [2]. A sensitivity analysis also proves that $\mu_t$ has limited effect on final results.

The governing equations consist of two sets of conservation equations of mass and momentum for gas and liquid phase, as well as a conservation equation of air mass fraction. Following Einstein summation convention with $j$ as the dummy index, and $i$ as the free index ($i = 1, 2$), the governing equations take the following form:

Gas-phase mass conservation equation:

$$\frac{\partial}{\partial x_j}(\alpha_g \rho_g u_{gj}) = -\dot{m} \tag{2}$$

Gas-phase momentum conservation equation:

$$\frac{\partial}{\partial x_j}(\alpha_g \rho_g u_{gj} u_{gi}) = \frac{\partial}{\partial x_j}(\alpha_g \mu_e \frac{\partial u_{gi}}{\partial x_j}) + \frac{\partial}{\partial x_j}(\alpha_g \mu_e \frac{\partial u_{gj}}{\partial x_i}) - \frac{2}{3}\alpha_g \mu_e \frac{\partial}{\partial x_i}(\frac{\partial u_{gj}}{\partial x_j}) - \alpha_g \frac{\partial p}{\partial x_i} - \dot{m} u_{gi} - \alpha_g F_{gi} + C_{fi}(u_{li} - u_{gi}) \tag{3}$$

Liquid-phase mass conservation equation:

$$\frac{\partial}{\partial x_j}(\alpha_l \rho_l u_{lj}) = \dot{m} \tag{4}$$

Liquid-phase momentum conservation equation:

$$\frac{\partial}{\partial x_j}(\alpha_l \rho_l u_{lj} u_{li}) = -\alpha_l \frac{\partial p}{\partial x_i} + \dot{m} u_{li} - \alpha_l F_{li} + C_{fi}(u_{gi} - u_{li}) + \delta_{i2}\alpha_l \rho_l g \tag{5}$$

Conservation of air (non-condensable gas phase) mass fraction:

$$\frac{\partial}{\partial x_j}(\alpha_g \rho_g Y_a u_{gj}) = \frac{\partial}{\partial x_j}(\alpha_g \rho_g D_e \frac{\partial Y_a}{\partial x_j}) \tag{6}$$

The gas phase volume fraction $\alpha_g$ is obtained from the definition of porosity:

$$\alpha_g + \alpha_l = \begin{cases} 1, & \text{untubed region} \\ \beta, & \text{tube bundle region} \end{cases} \tag{7}$$

According to assumption 2, the density of gas phase is obtained from the mixing law of the perfect gas:

$$Y_s = 1 - Y_a \tag{8}$$

$$\frac{1}{\rho_g} = \frac{Y_a}{\rho_a} + \frac{Y_s}{\rho_s} \tag{9}$$

where $\rho_a$, $\rho_s$ are constant for air and steam. Since the liquid phase only consists of condensate, its density $\rho_l$ is also considered a constant.

The mass source term, $\dot{m}$, represents the mass transfer from gas to liquid phase due to condensation, which also brings about momentum transfer. Condensation only occurs within the tube bundle region, while evaporation in the liquid phase is neglected. $F_{gi}$ and $F_{li}$ denote the local flow resistances induced by the tube bundle for the gas and liquid phases. $C_{fi}(u_{li} - u_{gi})$ represents the interphase friction between two phases. In the liquid-phase momentum equation, gravity is incorporated in the $y$ direction using the Kronecker delta function $\delta_{i2}$.

The effective viscosity, $\mu_e$, comprises both the laminar viscosity $\mu$ and the turbulent viscosity $\mu_t$. $\mu$ is defined as a constant corresponding to pure steam at the average pressure and temperature. As suggested by Zhang et al. [2], $\mu_t$ can be treated as a constant to reduce computational cost while maintaining reasonable simulation accuracy. The effective diffusivity of air in steam, $D_e$, also consists of laminar diffusivity $D$ and turbulent diffusivity $D_t$, with $D_t$ calculated based on the assumption $Sc_t = 1$.

$$\mu_e = \mu + \mu_t \tag{10}$$

$$D_e = D + D_t, \ \mathrm{D}_t = \frac{\mu_t}{\rho Sc_t} \tag{11}$$

### 2.3.2. Momentum source terms

The flow resistance contributed by the tube bundles is modeled using the following relationships:

$$F_{p,i} = \xi_{p,i} \rho_p u_{p,i} U_{m,p} \tag{12}$$

where $p$ and $i$ indicate different phases and directions, respectively. $\xi_{p,i}$ represents the pressure loss coefficient only exists in the tube bundle region, which is modeled by the expression suggested by Rhodes and Carlucci [32]:

$$\xi_{p,i} = 2\left(\frac{f_{p,i}}{P_t}\right)\left(\frac{P_t \beta}{P_t - D_o}\right)^2 \left(\frac{1-\beta}{1-\beta_t}\right)$$
$$f_{p,i} = \begin{cases} 0.619 \mathrm{Re}_{p,i}^{-0.198}; & \mathrm{Re}_{p,i} < 8000 \\ 1.156 \mathrm{Re}_{p,i}^{-0.2647}; & 8000 < \mathrm{Re}_{p,i} < 2 \times 10^5 \end{cases} \tag{13}$$
$$\mathrm{Re}_{p,i} = \frac{\rho_p u_{p,i} D_o}{\mu_p}$$

In this study, the interphase force considers only the friction caused by the relative motion between droplets and the gas phase. The friction is dependent on the relative velocity and the interphase friction coefficient, $C_{fi}$, which is expressed as:

$$C_{fi} = \frac{1}{2}\rho_g f_d A_d |u_{li} - u_{gi}|$$
$$A_d = \frac{1.5\alpha_l}{D_d} \tag{14}$$

where $A_d$ represents the total interphase area of droplets within the control volume, which is derived from the spherical droplet assumption, the diameter of droplets is taken as a constant $D_d = 0.001$ m. The drag force coefficient $f_d$ is calculated using the empirical equation proposed by Clift et al. [33], which is a function of droplet Reynold number $\mathrm{Re}_d$:

$$f_d = \frac{24}{\mathrm{Re}_d}(1 + 0.15\mathrm{Re}_d^{0.687}) + \frac{0.42}{1 + 4.25 \times 10^4 \mathrm{Re}_d^{-1.16}}, \mathrm{Re}_d < 3 \times 10^5$$
$$\mathrm{Re}_d = \frac{\rho_g D_d U_{m,rel}}{\mu_g} \tag{15}$$

here $U_{m,rel}$ denotes the magnitude of relative velocity between the gas and liquid phase.

### 2.3.3. Mass source term

The mass source term $\dot{m}$ represents the mass of steam condensed per unit volume. It is determined based on the energy balance between the latent heat released during condensation and the heat absorbed by the cooling water:

$$\dot{m} = \frac{T_s - T_{cw}}{R_{tot} L_{lg} V_c} A \tag{16}$$

The tube surface area $A$ within the control volume $V_c$ is dependent on the local number of tubes in each cell $n_t$. For the smooth round tubes, the relationship between $A$ and $n_t$ is expressed as follows:

$$A = n_t \pi D_o \tag{17}$$

Based on the assumption that steam and condensate are in the

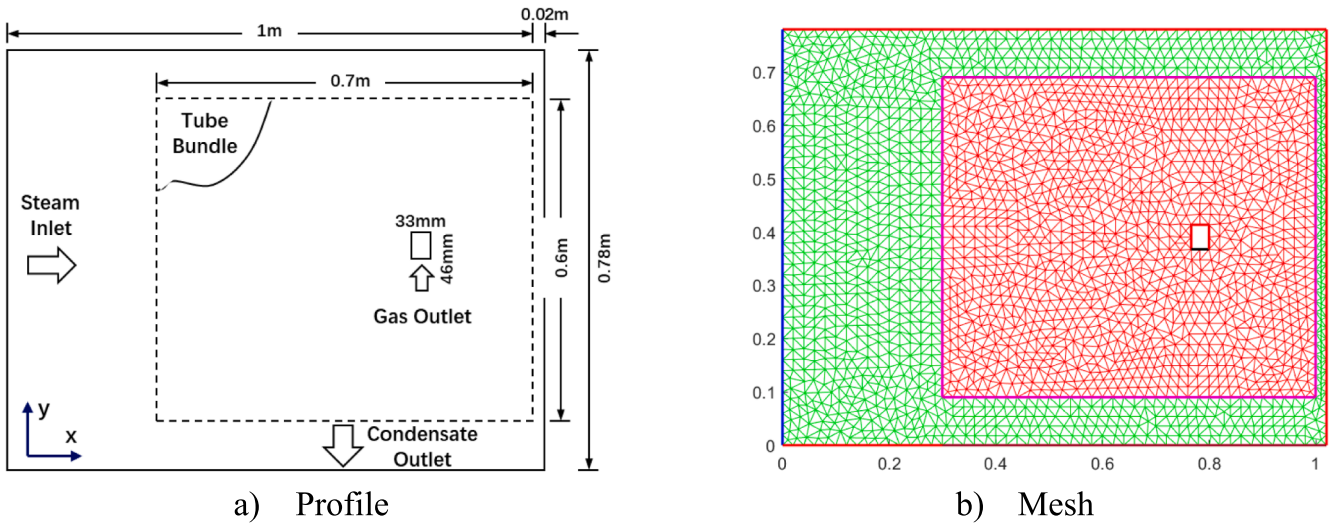


**Fig. 4.** Profile of the experimental condenser and the mesh used for simulation.

saturated state, local steam temperature $T_s$ is determined from the local partial steam pressure using the pressure–temperature correlation suggested by IAPWS-IF97 [34]. The local temperature rise of the cooling water from inlet to outlet in each mesh cell is calculated based on the local condensation rate. The local temperature difference between the cooling water and the steam for heat exchange is defined as the logarithmic mean temperature difference (LMTD):

$$\begin{aligned} \Delta T_{cw} &= T_{cw,out} - T_{cw,in} = \frac{\dot{m} V_c L_{\mathrm{lg}} \mathrm{Len}}{\dot{M}_{cw} c_{p,cw}} \\ T_s - T_{cw} &= \mathrm{LMTD} = \frac{\Delta T_{cw}}{\ln\left(\frac{T_s - T_{cw,in}}{T_s - T_{cw,out}}\right)} \end{aligned} \tag{18}$$

Cooling water flow rate in each mesh cell is re-calculated based on the number of tubes within the cell once the porosity is changed.

The total thermal resistance consists of four parts, representing a series of media between cooling water and steam:

$$R_{tot} = R_{cw} + R_t + R_a + R_c \tag{19}$$

The thermal resistance of cooling water $R_{cw}$ is calculated using the classic Ditus-Boelter correlation [35] for forced convection inside tubes:

$$\begin{aligned} R_{cw} &= \left(0.023 \frac{\lambda_{cw}}{D_i} \mathrm{Re}_{cw}^{0.8} Pr_{cw}^{0.4}\right)^{-1} \left(\frac{D_o}{D_i}\right) \\ \mathrm{Re}_{cw} &= \frac{\rho_{cw} U_{cw} D_i}{\mu_{cw}} \\ Pr_{cw} &= \frac{\mu_{cw} c_{p,cw}}{\lambda_{cw}} \end{aligned} \tag{20}$$

The thermal resistance of the tube wall $R_t$ is calculated using the following equation:

$$R_{\mathrm{t}} = \frac{D_{\mathrm{o}} \ln\left(\frac{D_{\mathrm{o}}}{D_{\mathrm{i}}}\right)}{2\lambda_{\mathrm{t}}} \tag{21}$$

The thermal resistance of air $R_a$ accumulated at the gas–liquid interface is calculated using the empirical correlation given by Berman and Fuks [36]:

$$\begin{aligned} R_{\mathrm{a}} &= \left[\mathrm{a} \frac{D_e}{D_{\mathrm{o}}} \mathrm{Re}_g^{1/2} \left(\frac{p}{p - p_{\mathrm{s}}}\right)^{\mathrm{b}} p^{1/3} \left(\rho_{\mathrm{s}} \frac{L_{\mathrm{lg}}}{T_s}\right)^{2/3} \frac{1}{(T_s - T_{\mathrm{ci}})^{1/3}}\right]^{-1} \\ \mathrm{Re}_g &= \frac{\rho_g U_{m,g} D_o}{\mu_s} \\ \mathrm{Re}_g &< 350,\ \mathrm{a} = 0.52,\ \mathrm{b} = 0.7 \\ \mathrm{Re}_g &> 350,\ \mathrm{a} = 0.82,\ \mathrm{b} = 0.6 \end{aligned} \tag{22}$$

where $p$ and $p_s$ are the total pressure of gas and partial pressure of steam, respectively; $T_s$ and $T_{ci}$ are temperatures of steam and gas–liquid interface, respectively. Under the assumption of a constant heat flux from the cooling water to the steam, the temperature rise across each thermal resistance is proportional to its share of the total thermal resistance.

The thermal resistance of condensate film $R_c$ could have a significant impact on the heat transfer characteristics, especially for the bottom tubes that are immersed in condensed water dripping down from the tubes above. To account for this, $R_c$ at different positions is assumed to be proportional to the liquid film thickness. Assuming that the liquid film thickness is proportion to the volume fraction of the liquid phase, an inundation correction proposed in this study is added to the vapor share correction given by Berman and Tumanov [37] :

$$\begin{aligned} \mathrm{Nu} &= \frac{\mathrm{h} D_{\mathrm{o}}}{\lambda_{\mathrm{c}}} = 0.728 \left[\frac{g L_{\mathrm{lg}} \rho_{\mathrm{c}} (\rho_{\mathrm{c}} - \rho_g) D_{\mathrm{o}}^3}{\mu_{\mathrm{c}} \lambda_{\mathrm{c}} (T_{\mathrm{ci}} - T_{\mathrm{ow}})}\right]^{\frac{1}{4}} \\ R_{\mathrm{c}} &= \left(\frac{\lambda_{\mathrm{c}}}{D_{\mathrm{o}}} \mathrm{Nu} \left(1 + 0.0095 \mathrm{Re}_{\mathrm{g}}^{11.8/\sqrt{\mathrm{Nu}}}\right)\right)^{-1} \max\left(\frac{\alpha_l}{C}, 1\right) \end{aligned} \tag{23}$$

where $T_{ci}$ and $T_{ow}$ are temperature of the gas–liquid interface and tube outer wall, respectively, which are determined by the corresponding thermal resistance ratio in $R_{tot}$. $C$ is a variable reflecting the liquid-phase volume fraction of the tubes unaffected by the liquid film thickening effect, which is taken as 0.001 in this study. $\frac{\alpha_l}{C}$ equals to the thermal resistance ratio of any tube to the tube without inundation effect. The maximum function with 1 ensures that the minimum correction equals to the tube without inundation.

### 2.4. Particle swarm optimization algorithm

Engineering optimization problems are typically formulated as mathematical models aimed at finding the optimal values of the objective functions subject to specific constraints. In this study, the optimization focuses on the flow and heat transfer performance of the

**Table 1**
Original geometric and operating parameters of the experimental condenser.

| Geometric parameters | Unit | Value |
|---|---|---|
| Condenser Length | m | 1.219 |
| Condenser Width | | 1.02 |
| Condenser Height | m | 0.78 |
| Tube Outer Diameter | mm | 25.40 |
| Tube Wall Thickness | mm | 1.25 |
| Tube Pitch | mm | 34.90 |
| Operating Condition | | |
| Inlet Cooling Water Temperature | °C | 17.80 |
| Inlet Cooling Water Velocity | m/s | 1.19 |
| Inlet Steam Pressure | pa | 27,670 |
| Inlet Steam Flow Rate | kg/s | 2.032 |
| Inlet Air Flow Rate | kg/s | $2.48 \times 10^{-4}$ |

condenser, which are derived from the CFD simulation results. Since these objective functions are non-differentiable and the relationship between design variables and the objectives is implicit, an evolutionary algorithm is adopted to address such problems.

Particle Swarm Optimization (PSO) [38] is a widely used evolutionary algorithm in engineering optimization. Inspired by the social behavior of flocks and swarms, PSO starts with randomly initializing a group of particles in the search space, each with a position and velocity. The position of a particle represents a potential solution of design variables. During each iteration, particles explore the search space by updating their positions based on their velocities and evaluate the objective function at the new positions. To guide the search, the algorithm keeps track of both the best position found by each individual particle (personal best) and the best position found by the entire swarm (global best). Each particle adjusts its velocity according to both its personal experience and group knowledge of the optimal position and updates its position along the direction of velocity.

Mathematically, PSO algorithm updates velocities and positions of particles using the following equations:

$$\mathbf{v}_k^{t+1} = \omega^{t+1}\mathbf{v}_k^t + c_1 \mathrm{r}_1(\mathbf{p}_k^t - \mathbf{x}_k^t) + c_2 \mathrm{r}_2(\mathbf{g}^t - \mathbf{x}_k^t) \tag{24}$$

$$\mathbf{x}_k^{t+1} = \mathbf{x}_k^t + \mathbf{v}_k^t \tag{25}$$

where $k = 1, 2, \ldots, K$ denotes the particle index and $t = 1, 2, \ldots, T$ is the iteration step. $\mathbf{v}_k^t, \mathbf{x}_k^t, \mathbf{p}_k^t, \mathbf{g}^t \in \mathbb{R}^D$ are vectors with dimensionality D equals to the number of design variables. $c_1, c_2$ are cognitive and social coefficients adjusting the influence of personal best and global best position on the velocity. $\mathrm{r}_1, \mathrm{r}_2$ are random numbers between 0 and 1 that exert stochastic influence on the search process enabling the particles to escape from local optima. $\omega^t$ is the inertial weight to control the influence of the previous velocity on the current one to avoid divergence, a linearly decreasing strategy (26) is employed in this work to dynamically adjust inertial weight across iteration steps. A large inertial weight $\omega^0 = 0.9$ is adopted at the initial stage to favor global search, and it decreases to a small value $\omega^T = 0.4$ at the end to favor local search.

$$\omega^{t+1} = \omega^T + (\omega^0 - \omega^T)\frac{(T-t)}{T} \tag{26}$$

## 3. Results and discussion

### 3.1. Target condensers and computation method

In this study, the CFD solver is validated with the measured data [39]

**Table 2**
Original geometric and operating parameters of the industrial condenser.

| Geometric parameters | Unit | Value |
|---|---|---|
| Condenser Length | m | 7.30 |
| Tube Outer Diameter | mm | 19.05 |
| Tube Wall Thickness | mm | 0.70 |
| Tube Pitch | mm | 26.00 |
| Operating Condition | | |
| Inlet Cooling Water Temperature | °C | 20.00 |
| Inlet Cooling Water Velocity | m.s | 1.19 |
| Inlet Steam Pressure | pa | 7500 |
| Inlet Steam Flow Velocity | m/s | 45.00 |

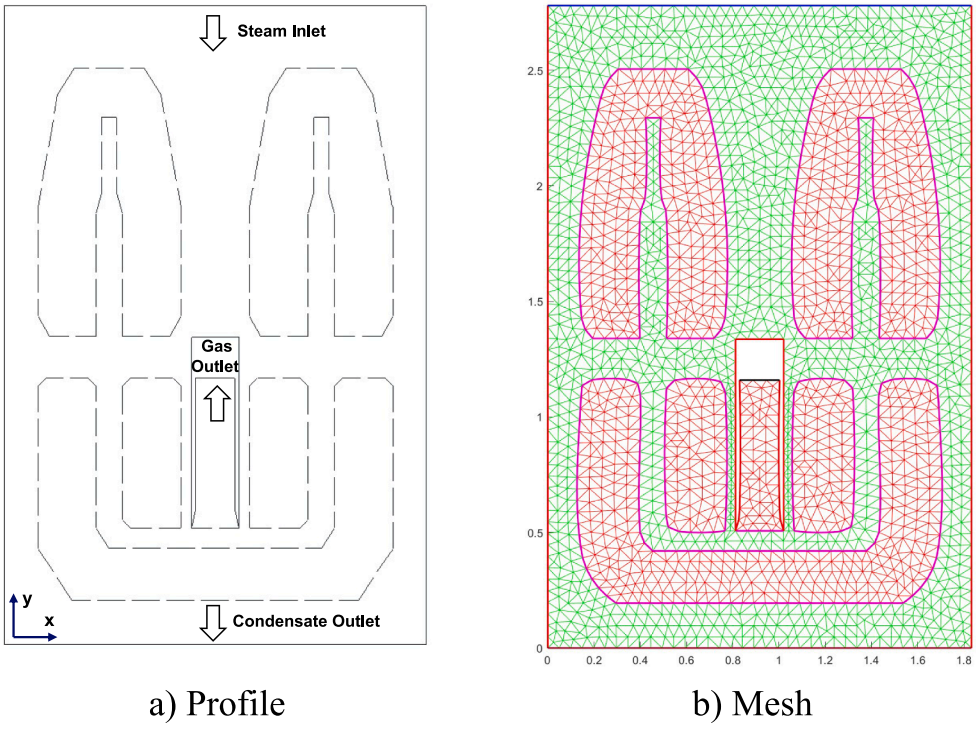


**Fig. 5.** Profile of the industrial condenser and the mesh used for simulation.

**Table 3**
Mesh independence verification of key performance metrics of the experimental condenser.

| Cell number | Uncondensed ratio | HTC* |
|---|---|---|
| | % | $W \bullet m^{-2} \bullet K^{-1}$ |
| 808 | 0.86 | 2626 |
| 1902 | 0.37 | 2637 |
| 4574 | 0.30 | 2639 |

* HTC: (averaged) Heat Transfer Coefficient.

**Table 4**
Mean absolute percentage error of numerical heat flux value along four rows of tubes.

| | 3rd Row | 8th Row | 13th Row | 18th Row |
|---|---|---|---|---|
| Our Simulation | 10.02 % | 24.08 % | 17.18 % | 25.36 % |
| Zhang 1997[4] | 20.51 % | 23.01 % | 17.88 % | 25.49 % |

of an experimental condenser widely used in literatures [2,3]. The ReSONS method is applied to this experimental condenser as well as an industrial condenser reported by Naviglio [40].

The profile and mesh of the experimental condenser are illustrated in Fig. 4. In its original design, 400 tubes are uniformly arranged within the rectangular tube bundle region in a triangular layout. The geometric and operating parameters of this condenser are summarized in Table 1. The profile and mesh of the industrial condenser are illustrated in Fig. 5. 3968 tubes are uniformly arranged in a triangular layout. The geometric and operating parameters are summarized in Table 2.

The homemade 2-D condenser CFD calculation program, ConDesign-2D, is used as the CFD solver to be integrated with PSO algorithm. Both CFD solver and optimization algorithm are developed based on MATLAB. The program solves the two-fluid model through the finite volume method on unstructured collocated mesh using SIMPLE algorithm. Rhie-Chow interpolation method is adopted to solve the velocity–pressure decoupling problem. The convection term is discretized in a first order upwind scheme. The gradients of flow variables at the cell centers are calculated with the Green-Gauss method. The source terms are discretized with Gaussian integration using their values at cell centers. Unstructured meshes are generated by the open-source program 'bamg' [41] to adapt to the complex shape of the condenser.

The numerical model employs the following boundary conditions: At the inlet, the air mass fraction and velocity are specified for both gas and liquid phases, with the liquid phase volume fraction set to a small value. The gas outlet is defined by a specified pressure condition. The bottom wall serves as an outlet for the liquid phase, whereas the gas phase encounters a no-slip wall. For all remaining walls, a no-slip condition is applied to both gas and liquid phases.

Each CFD simulation of the experimental condenser, using a mesh with 1902 cells, takes about 10 min on average when run on an Intel® Xeon® Platinum 8336C processor. Since the CFD simulations for different particles within the same optimization iteration are independent, they can be executed in parallel. By utilizing 16 workers in a parallel computing pool, the total computation time for a complete

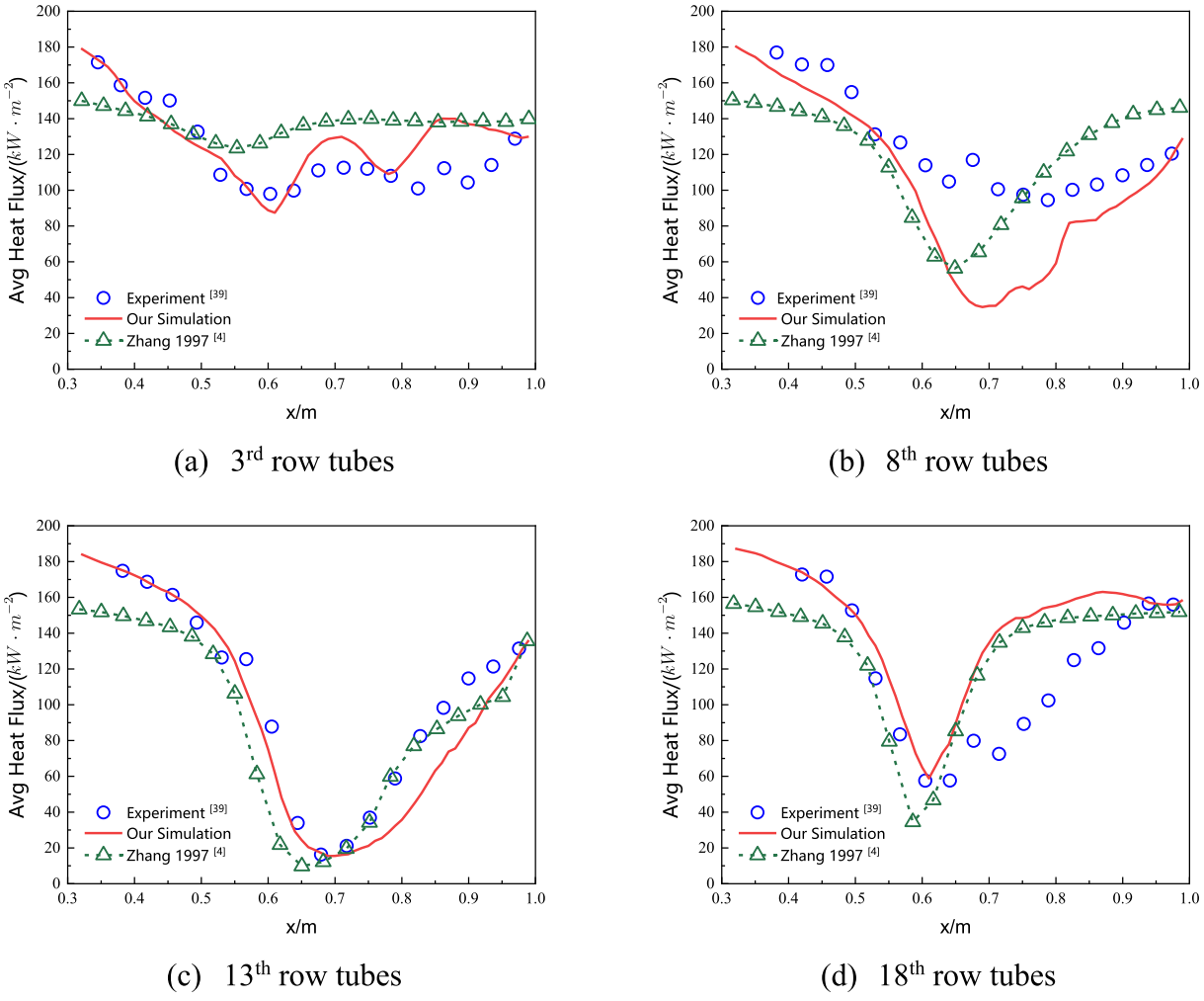


**Fig. 6.** Comparison of heat flux between numerical and experimental value along four rows of tubes.

**Table 5**
PSO parameters used for the regional optimization.

| Parameter | Value | Parameter | Value |
|---|---|---|---|
| Population | 24 | Cognitive Coeff $c_1$ | 1 |
| Iteration | 20 | Social Coeff $c_2$ | 2 |

optimization process involving 480 CFD simulations can be reduced to less than 24 h.

### 3.2. CFD solver validation

Table 3 lists the calculation results of the experimental condenser with different number of cells. Key physical quantities only changs slightly when the number of cells increases from 1902 to 4574, so the 1902 mesh is considered to be sufficiently fine to meet the mesh independence requirement.

To validate the accuracy of the developed solver, simulations were conducted based on the original design parameters of the experimental condenser, and the results were compared with experimental data [39] and the simulation results provided by Zhang et al [4]. The average heat flux for four rows of tubes, from bottom to top, was extracted from our simulation result and compared with the measurements. The mean absolute percentage errors of the predicted heat flux are listed in Table 4. As shown in Fig. 6, The accuracy of the lower rows of tubes is higher than that of the upper row of tubes. Despite the deviation of 8$^{th}$ row at $x \in [0.6, 0.8]$ and 18$^{th}$ row at $x \in [0.7, 0.9]$, the overall trend of the heat flux aligns well with the experimental data, demonstrating reasonable simulation capability of the solver. Our predicted total condensation rate is 2.025 kg/s, which also fits well with the measurement of 2.021 kg/s [4].

### 3.3. Results of the experimental condenser

This study focuses on enhancing condensation efficiency and reducing steam flow resistance through optimizing tube density. When the tube bundle region is modeled as porous media, the tube density is directly reflected by the regional porosity values, which are used as the design variables. The objective function to be minimized during optimization is composed of two performance metrics:

$$f(\beta) = \frac{\Delta p_s}{\dot{m}} \tag{27}$$

where $\Delta p_s$ is the shell-side pressure drop from inlet to outlet, reflecting the steam flow resistance. The inlet pressure is obtained as the area-weighted-average pressures on the inlet boundary faces, and $\Delta p_s$ is calculated as the difference between the inlet and outlet pressures. Reducing flow resistance improves equipment vacuum levels, and lowers condensate subcooling and oxygen content. $\dot{m}$ is the condensation rate defined as the mass of steam condensed in the condenser per unit time, which should approach the inlet mass flow rate to ensure efficient operation.

$\beta = (\beta_1, \beta_2, ..., \beta_n)$ are regional porosities to be optimized. The searching space for each porosity value is restricted to $(0.2146, 0.99)$, corresponding to pitch value $P_t = 5D_o$ and $P_t \approx \infty D_o$ respectively. PSO parameters listed in Table 5 are used by default.

#### 3.3.1. Comparison of regional split optimization with original design and global optimization

To evaluate the effectiveness of the proposed regional split optimization method, the tube bundle was first divided into 3 × 3 subregions with 9 independent porosity variables. This approach was compared with optimizing the global porosity value without splitting the tube bundle region. Additionally, the performance metrics of the condenser optimized using the 3 × 3 regional split and global porosity approaches were compared to those of the original design. A total of 20 optimization iterations were performed using a particle swarm with 24 particles. The resulting performance metrics for all cases are summarized in Table 6.

As shown in Case 0 and Case 1, the performance metrics and objective function values obtained from global optimization are nearly equal to those of the original design. This indicates that, under a conventional uniform tube bundle arrangement, the original design was already close to optimal, leaving limited room for further optimization.

In contrast, by dividing the tube bundle into 9 independent subregions and optimizing the porosity of each region, further performance gains were achieved. As shown in Case 2, the objective function value decreased from 30.08 in the original design to 22.39 with the 3 × 3 partition. Compared with the global optimized design, the 3 × 3 regional split optimization reduced the steam pressure drop by approximately 23 %, and the uncondensed ratio by about 36 %. These improvements in both flow and heat transfer performance demonstrate the potential of the regional split optimization approach to overcome the limitations of conventional uniform tube arrangements.

#### 3.3.2. Comparison between different region partitions

Building on the success of the 3 × 3 regional split optimization, further investigations were carried out to access the impact of finer partitioning on condenser performance. The tube bundle region was

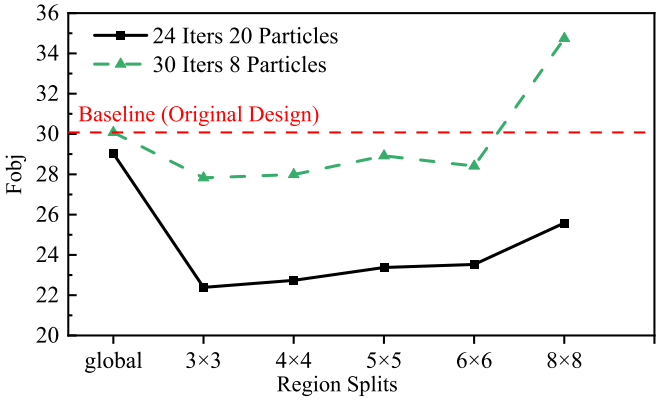


**Fig. 7.** The trend of the optimal objective function changing with the number of subregions. The objective function under fine split deteriorates due to insufficient search of parameter space.

**Table 6**
Optimal performance metrics of experimental condenser under 20 iterations of 24 particles with different region splits.

| | Configuration | Uncondensed ratio | Pressure drop | HTC | Objective function |
|---|---|---|---|---|---|
| | | % | Pa | W • m$^{-2}$ • K$^{-1}$ | Pa • s • kg$^{-1}$ |
| Case 0 | Original | 0.49 | 60.81 | 2632 | 30.08 |
| Case 1 | Global Opt | 0.45 | 58.71 | 2730 | 29.03 |
| Case 2 | 3 × 3 Opt | 0.29 | 45.36 | 2327 | 22.39 |
| Case 3 | 4 × 4 Opt | 0.18 | 46.12 | 2372 | 22.74 |
| Case 4 | 5 × 5 Opt | 0.31 | 47.36 | 2519 | 23.38 |
| Case 5 | 6 × 6 Opt | 0.23 | 47.70 | 2381 | 23.53 |
| Case 6 | 8 × 8 Opt | 0.23 | 51.87 | 2651 | 25.59 |

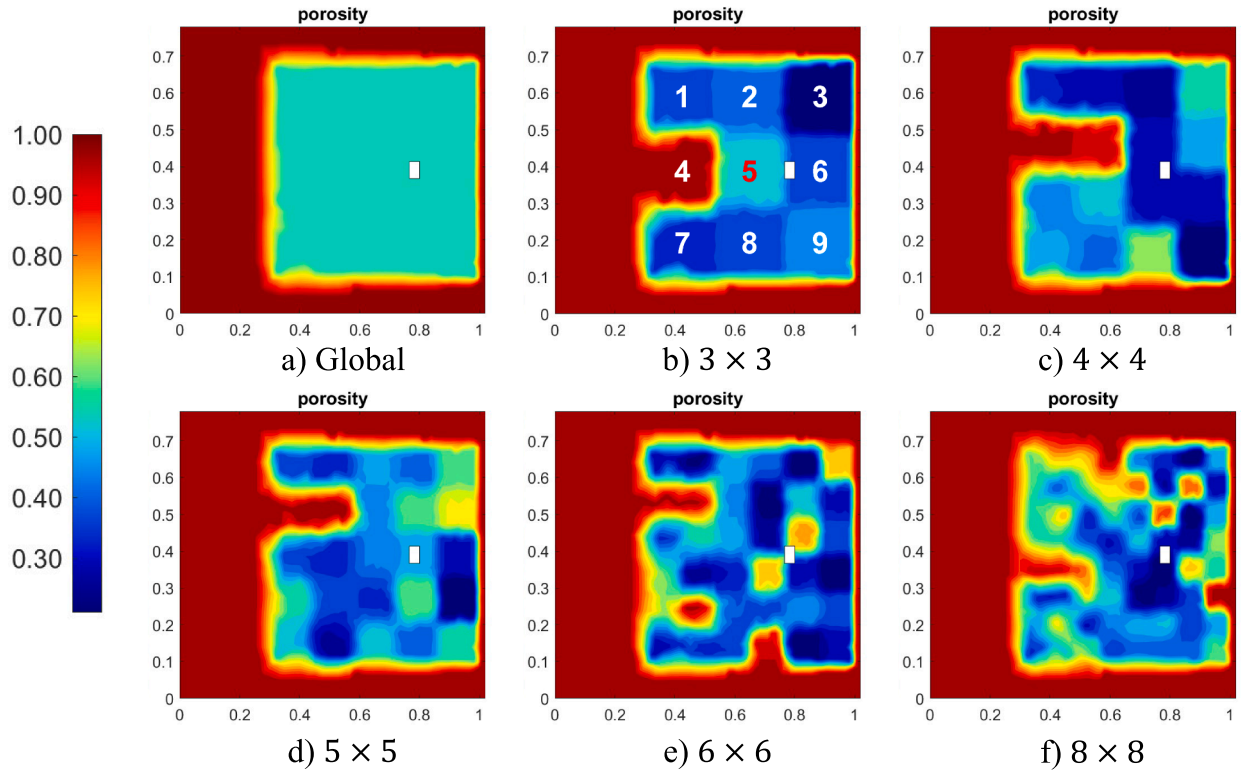


**Fig. 8.** Optimized porosity distribution under different region splits. The optimization results show a similar high porosity region on the upstream periphery.

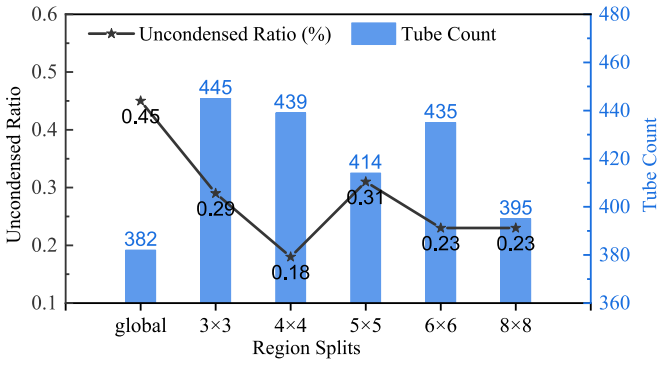


**Fig. 9.** The tube count and uncondensed ratio for different region splits.

divided into progressively smaller subregions, ranging from 4 × 4 to 8 × 8, with the aim of achieving more refined designs.

The corresponding performance metrics for these finer partitions are summarized in Table 6. The results show that finer partitions still can provide better performance than the uniform tube arrangement. The 4 × 4 partition achieved the lowest uncondensed ratio, reducing it by 63 % compared to the original design. Meanwhile, the 3 × 3 partition yielded the lowest pressure drop, representing a 25 % reduction from the original design.

Fig. 7 shows the trend of the objective function with increasing number of subregions. The solid line represents the results obtained using 24 particles over 20 iterations, while the dushed line shows results form 8 particles over 30 iterations for comparison. As the number of subregions increases, the objective function exhibits a slight increase trend. This performance degradation is attributed to the growing complexity of the optimization problem in higher-dimensional design space. The discrepancy between the two lines in Fig. 7 shows that the optimization effect is closely related to the search capability of optimizer. When only 8 particles are employed, the deterioration with increasing dimensionality becomes more pronounced, with the objective function for the 8 × 8 partition even exceeding that of the original design. Upon increasing the number of particles to 24, the results of the 8 × 8 partition improve significantly. However, the resulting porosity distributions in these finer partitions tends to become excessively intricate, deviating from practical engineering feasibility.

The optimized porosity distributions under different partitioning schemes are shown in Fig. 8. The improvement in condenser performance has a close relationship with the spatial patterns of porosity. As shown in Fig. 8 b), the porosity in region 4 of 3 × 3 partition, located at the center of the steam inlet side, is significantly higher than the surrounding regions. This implies a lower tube bundle density in this region, resulting in wider tube spacing and a larger flow area on the upstream periphery. Such a design reduces flow resistance to the incoming steam, facilitating better steam diffusion into the interior of the tube bundle. A similar pattern emerges across all finer partitions, where high-porosity regions appear in the middle or upper part of the bundle on the steam inlet side. When the high-porosity region is located in the upper region, it can reduce the flow resistance from the upper tube bundle to the downward-facing outlet.

Notably, this optimized tube arrangement, which reduces tube density on the upstream periphery, aligns with established engineering practices. In industrial condenser designs, inlet steam channels are commonly employed to enhance steam diffusion. ReSONS optimization reveals a similar pattern purely through CFD data-driven optimization, without relying on prior knowledge.

Fig. 9 shows the total number of tubes calculated from the optimized porosity and the corresponding uncondensed ratio. The original configuration contains 400 tubes (with a computed value of 397) and has an uncondensed ratio of 0.49 %. The 4 × 4 partition achieves the lowest uncondensed ratio, while the number of tubes increased by about 10 %. However, a greater number of tubes does not necessarily guarantee a lower uncondensed ratio. Compared to 3 × 3 partition, the 4 × 4 partition achieves a lower uncondensed ratio with fewer tubes through more reasonable arrangement.

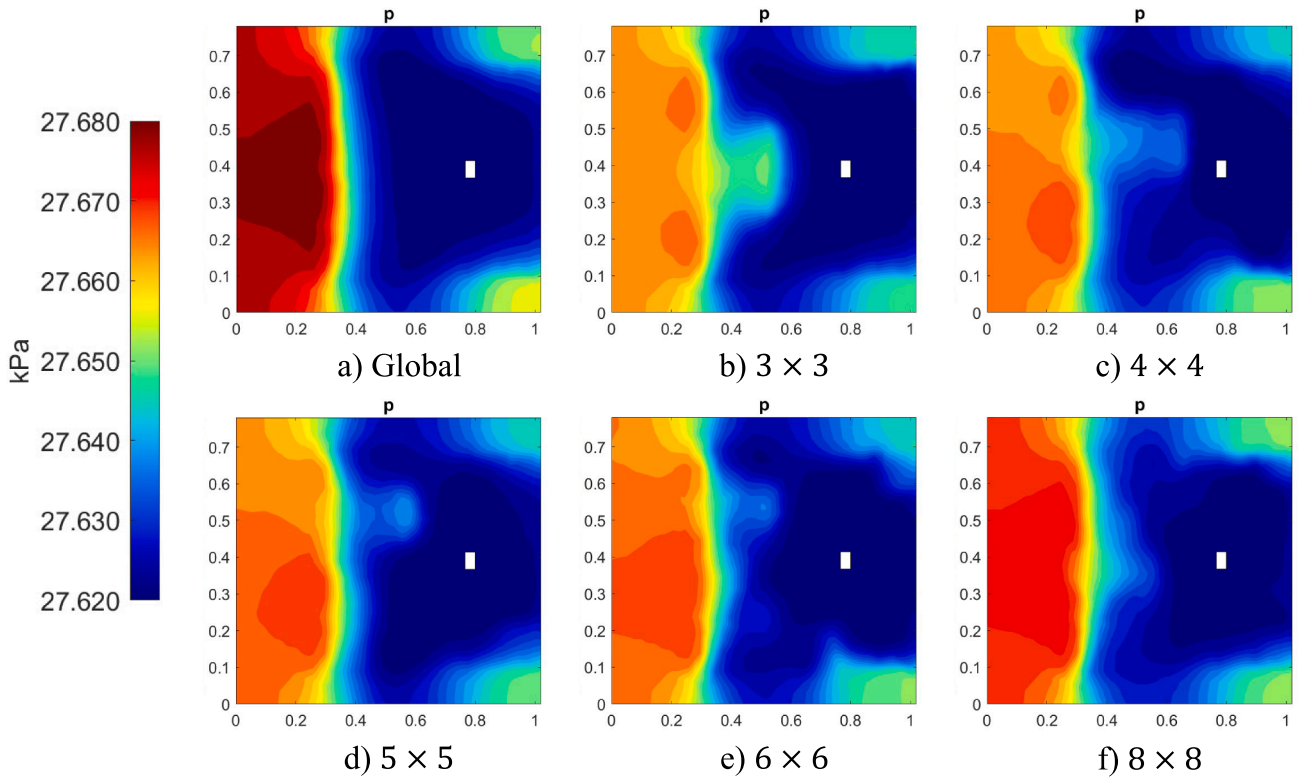


**Fig. 10.** Pressure distribution under different region splits. High porosity region on the upstream periphery results in a lower pressure gradient.

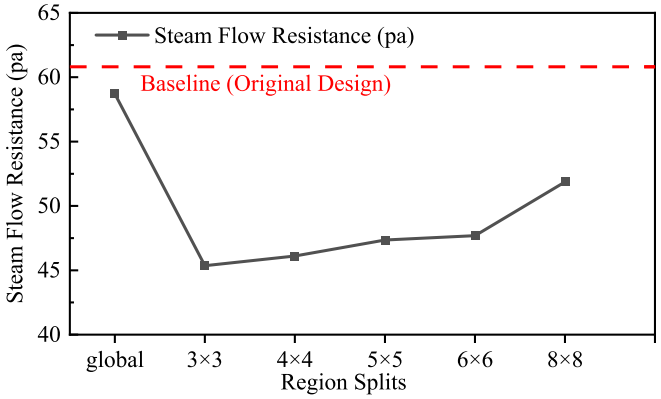


**Fig. 11.** The steam flow resistance for different region splits.

Fig. 10 and Fig. 11 shows the impact of porosity distribution on the pressure field and steam flow resistance across different partitions. The pressure drop within the tube bundle is primarily caused by two factors: the flow resistance of the tube bundle and the steam condensation. In the uniform arrangement of tube bundles (Fig. 10 a)), the high tube density near the periphery of the tube bundle region leads to intense condensation and restricted flow passages. This results in a substantial pressure drop and the formation of an extensive low-pressure zone within the bundle. This phenomenon contributes to high steam flow resistance and impedes the effective diffusion of steam into the interior. In contrast, the partitioned optimization designs exhibit higher porosity regions along the upstream periphery of the tube bundle, which reduces the local condensation rate and increases the flow area. Consequently, these regions exhibit a gentler pressure gradient, leading to a reduction in steam flow resistance compared to the uniform arrangement.

Fig. 12 shows the distribution of surface Heat Transfer Coefficients (HTC) across different partitions. The results reveal that regions with higher porosity exhibit larger HTC values. Since HTC is the reciprocal of the total thermal resistance $R_t$, its spatial variation reflects the local heat transfer efficiency. Among the components of thermal resistance, the resistances from the tube bundle $R_{tb}$ and the cooling water $R_{cw}$ are independent of the shell-side flow conditions. Additionally, the air thermal resistance $R_a$ near the upstream periphery remains relatively stable. Therefore, the primary reason for the elevated HTC in high-porosity regions is a reduction in condensate thermal resistance $R_c$, which is a result of the high steam Reynolds numbers due to reduced flow resistance. However, as condensation proceeds, the local air concentration rises, leading to a rapid increase in $R_a$. This results in lower HTC values in the central regions of the tube bundle.

### 3.4. Results of the industrial condenser

The objective function for the industrial condenser is defined as a weighted sum of three components. First, the ratio of shell-side pressure drop $\Delta p_s$ to condensation rate $\dot{m}$ is included. Second, to control the construction costs, the number of tubes after optimization should not increase significantly. Conversely, an excessively low tube count may degrade the condensation efficiency, which is also undesirable. Therefore, a penalty term is added to constrain the total number of tubes, ensuring it does not deviate substantially from the original design value (3968). Third, during the optimization process, certain poor design parameter combinations may lead to non-convergent CFD simulations. These cases typically yield large objective function values. To mitigate their adverse impact on the optimization process, an additional penalty term is imposed on such cases to eliminate them in the early stage of optimization. Above all, the objective function of the industrial condenser takes the following form:

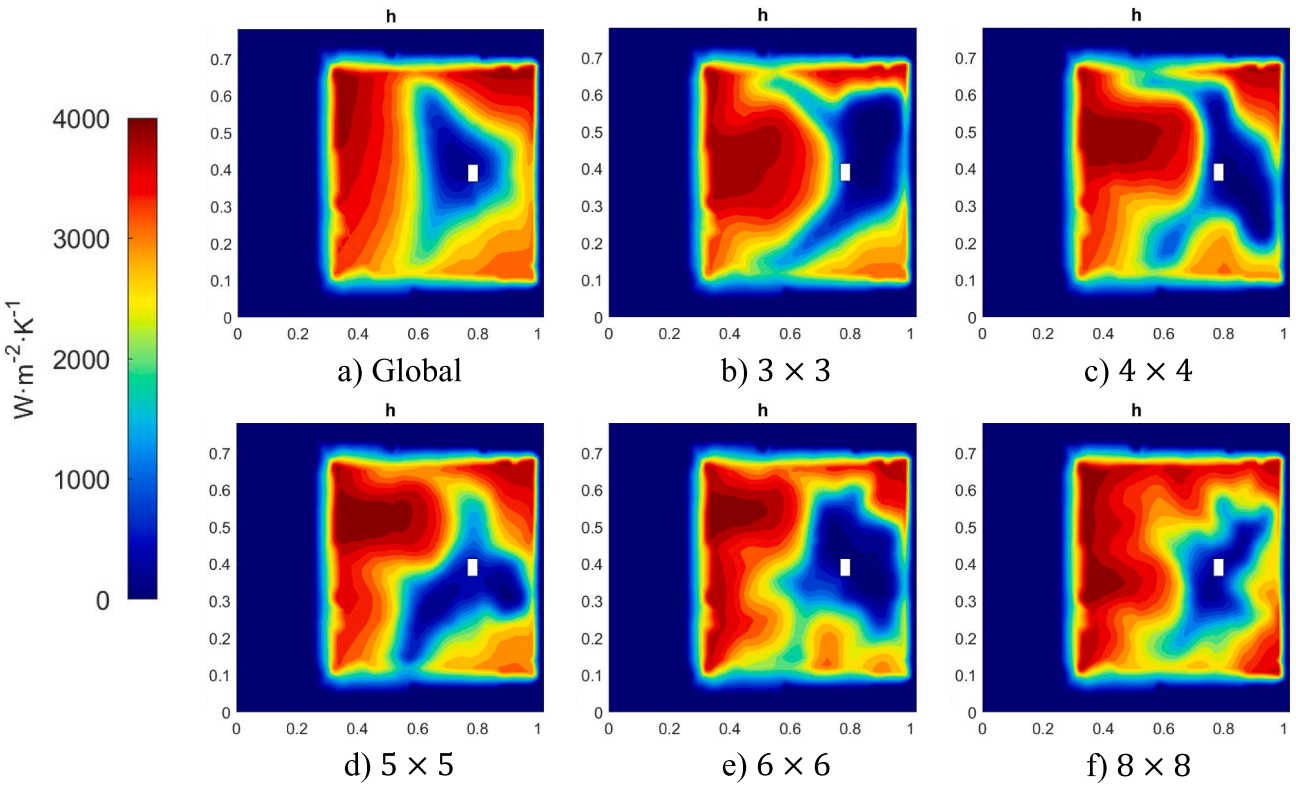


**Fig. 12.** Surface Heat Transfer Coefficient (HTC) distribution under different region splits. High porosity region on the upstream periphery has larger HTC due to the reduced $R_c$.

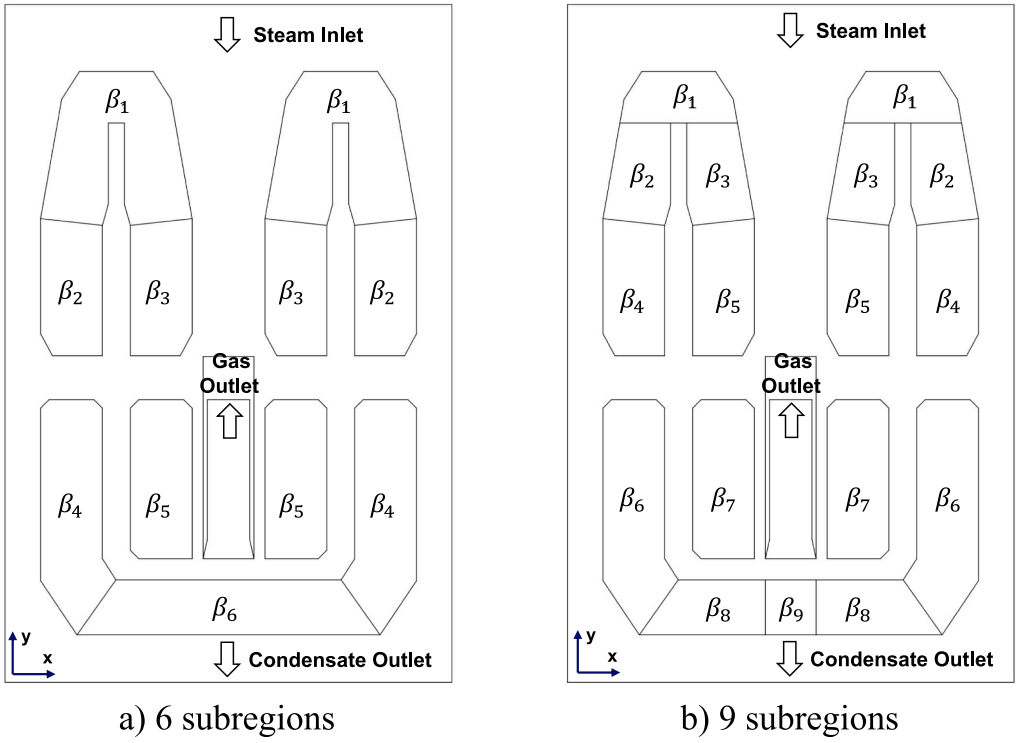


**Fig. 13.** Regional split of the industrial condenser and the correspondence of porosity variables.

**Table 7**
Optimal performance metrics of experimental condenser under 20 iterations.

| Configuration | Uncondensed ratio | Steam flow resistance | Computed tube count | Objective function |
|---|---|---|---|---|
| | % | Pa | \ | $Pa \bullet s \bullet kg^{-1}$ |
| Original | 3.81 | 1988 | 3973 | 66.89 |
| Global | 3.75 | 1948 | 3999 | 65.49 |
| 6-Opt | 3.09 | 1526 | 3999 | 50.96 |
| 9-Opt | 3.19 | 1586 | 4007 | 53.02 |

$$f(\beta) = w_1\frac{\Delta p_s}{\dot{m}} + w_2(\max(0, N_{\min} - N_t) + \max(0, N_t - N_{\max})) + w_3\mathbf{1}_{NC}$$
$$\mathbf{1}_{NC} = \begin{cases} 1, & \text{if } R_p > 1e-4 \text{ or } R_U > 1e-2 \text{ or } R_{Y_a} > 1e-2 \\ 0, & \text{otherwise} \end{cases} \tag{28}$$

where $N_{\min}$, $N_{\max}$ are minimum and maximum number of tubes desired. $R_\phi$ is the relative residual of corresponding equation. In this study, $[N_{\min}, N_{\max}] = [3950, 4000]$, $[w_1, w_2, w_3] = [1, 0.1, 100]$.

Given the symmetry of the condenser, the number of subregions with independent porosity variables is counted as half of the condenser. Two regional split schemes are considered, with 6 and 9 independent subregions, respectively. The splits of subregions are illustrated in Fig. 13. A global optimization case is also conducted to compare the effect with regional optimization.

The performance metrics before and after optimization are summarized in Table 7. All optimization results were obtained after 20 iterations using 24 particles. Similar to the previous case, the performance improvement under global optimization is negligible. In contrast, the two regional split cases show significant enhancements. Especially the case with 6 independent subregions achieves a notable reduction in the uncondensed ratio by 0.72 % and a decline in steam pressure drop by 462Pa, which is much better than the global case. Meanwhile, the total number of tubes in the 6-subregions design remains the same as in the global optimization result. It means that a uniform tube arrangement is not optimal, through rearranging the tube density, the performance of condenser can be significantly improved without increasing construction costs.

The performance of the 9-subregions case is not as good as the 6-subregions one, even though the design space of the 9-subregions case can be viewed as a refinement of the 6-subregions space, and the solutions of the latter form a constrained subset of the former. This indicates that the deterioration of the 9-subregions case is due to inadequate optimization rather than the limitations of the regional split method.

The optimized porosity values are summarized in Table 8, where the corresponding tube pitch given the outer diameter of 19.05 mm are also listed. The porosity distributions are illustrated in Fig. 14. Since the industrial condenser has already reserved steam channels and the top tube bundle area has no lateral partition on the upwind side, the optimized porosity distribution does not show high porosity subregions similar to the previous case.

Fig. 15 shows the pressure distribution for the global optimization

**Table 8**
The original and optimized regional porosity and corresponding tube pitch of industrial condenser.

| $i$ | | 1 | 2 | 3 | 4 | 5 | 6 | 7 | 8 | 9 |
|---|---|---|---|---|---|---|---|---|---|---|
| Original | $\beta_i$ | 0.513 | | | | | | | | |
| | $P_{ti}\,(mm)$ | 26.0 | | | | | | | | |
| Global | $\beta_i$ | 0.510 | | | | | | | | |
| | $P_{ti}\,(mm)$ | 25.9 | | | | | | | | |
| 6-Opt | $\beta_i$ | 0.483 | 0.456 | 0.562 | 0.613 | 0.539 | 0.335 | \ | \ | \ |
| | $P_{ti}\,(mm)$ | 25.2 | 24.6 | 27.4 | 29.1 | 26.7 | 22.2 | \ | | \ |
| 9-Opt | $\beta_i$ | 0.445 | 0.450 | 0.681 | 0.377 | 0.514 | 0.552 | 0.579 | 0.395 | 0.417 |
| | $P_{ti}(mm)$ | 24.3 | 24.5 | 32.1 | 23.0 | 26.0 | 27.1 | 28.0 | 23.3 | 23.8 |

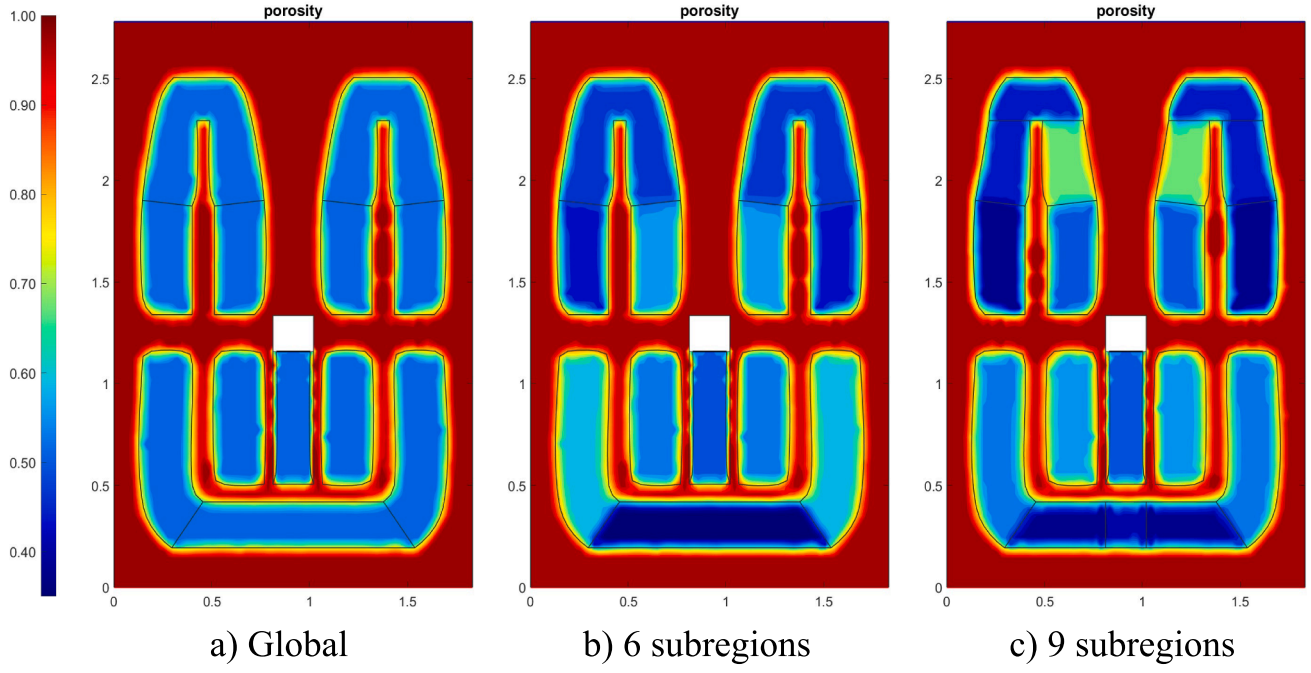


**Fig. 14.** Optimized porosity distribution under different region splits. The 6 subregions case gained the best performance among the three cases.

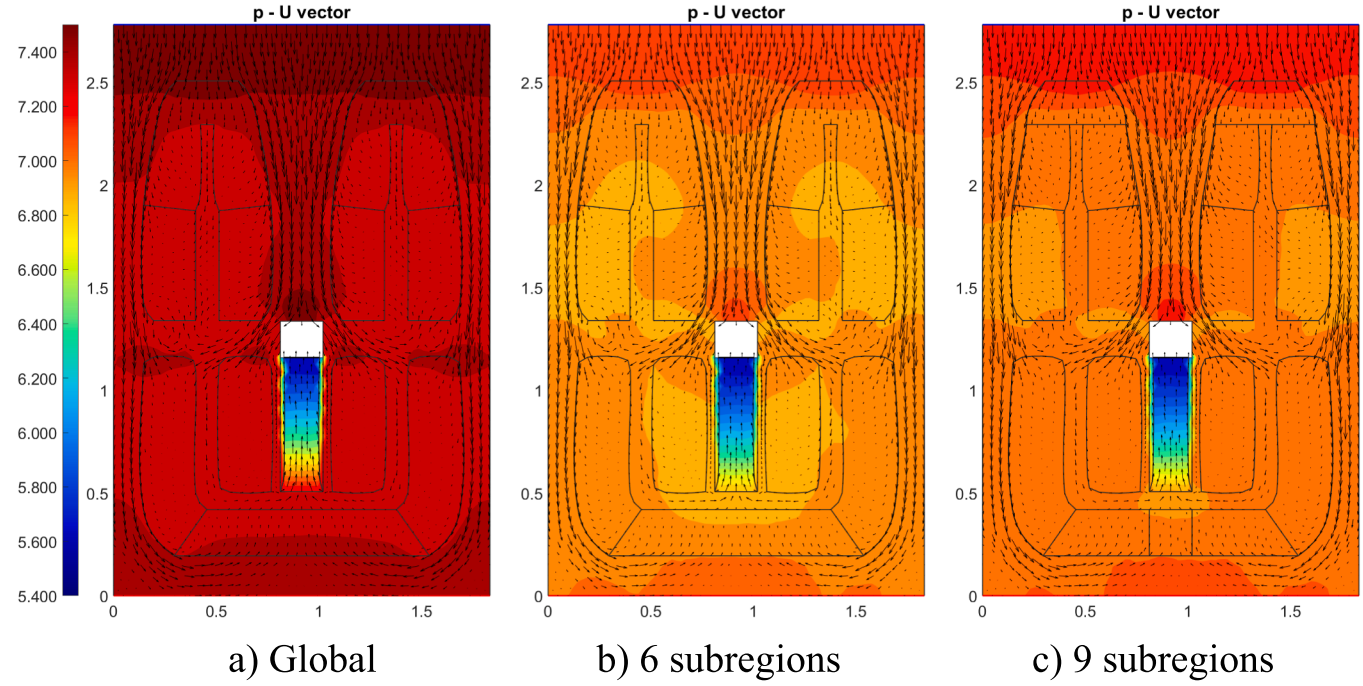


**Fig. 15.** Pressure distribution and steam velocity vector under different regional splits. The overall pressure of the regional optimization cases is lower due to higher condensed ratio.

and regional optimization results. Since the outlet pressure is fixed, the increased condensed ratio achieved in the 6-subreigons optimization leads to a lower inlet pressure, which is the main reason of the lower pressure drop. In the regional optimization cases, the average tube density in the top and bottom bundles is higher than that of the global optimization case. These regions are main flow paths of the steam. Specifically, the number of tubes in the top bundle increases from 1986 in the global optimization case to 2042 in the 6-subregion optimization result, which enhance steam condensation but also introduces slightly higher local flow resistance.

## 4. Conclusion

In this study, a Regional Split Optimization with Numerical Simulation (ReSONS) method is proposed to enable more flexible and locally informed optimization of condenser tube bundles. By coupling a two-dimensional multiphase CFD solver with the PSO algorithm, the method optimizes the porosity distribution across subregions of the tube bundle. This regional parameterization allows the optimization process to incorporate detailed flow and heat transfer characteristics given by CFD results, addressing the limitations of traditional global design approaches. In an experimental condenser case, the best results obtained from the ReSONS method reduce the pressure drop by 25 % and uncondensed ratio by 63 %, compared to the uniform tube arrangement. And in an industrial condenser case, the pressure drop and uncondensed ratio are reduced by 23 % and 19 %, respectively. These improvements highlight the method's ability to enhance design performance by expanding the design space and enabling localized control of tube bundle properties. Notably, the optimized tube bundle layout of the experimental condenser exhibits high porosity regions near the inlet to reduce flow resistance and facilitate steam diffusion, which is similar to engineering intuition. It demonstrates that ReSONS can generate physically meaningful and practical design insights.

This work presents a novel approach to integrating CFD-derived flow information into automated condenser design, providing a new pathway for localized optimization that bridges the gap between detailed simulation data and practical design strategies. However, increasing the number of subregions raises the dimensionality of the optimization problem. While a finer split may offer greater flexibility and potentially better solutions, the higher dimensionality also increases optimization difficulty, which can degrade performance under limited computational resources. Optimization under high degrees of freedom remains a challenging issue, future research should focus on the selection of optimization algorithms and strategies to better handle high-dimensional search spaces and avoid local optima.

## CRediT authorship contribution statement

**Ruihan Zhang:** Writing – original draft, Methodology. **Yuxin Wu:** Writing – review & editing, Supervision, Conceptualization. **Xiongshi Wang:** Software, Methodology. **Shoubao Dai:** Project administration, Conceptualization. **Tengteng Zhan:** Validation, Conceptualization. **Guihua Zhang:** Visualization, Software. **Junfu Lyu:** Supervision.

## Declaration of competing interest

The authors declare that they have no known competing financial interests or personal relationships that could have appeared to influence the work reported in this paper.

## Acknowledgement

This work was supported by Carbon Neutrality and Energy System Transformation program (CNEST) led by Tsinghua University, Huaneng Group Science and Technology Research Project (HNKJ23-H71-U23GCZH03), and the Fundamental Research Funds for the Central Universities (2022ZFJH004).

## Data availability

Data will be made available on request.

## References


[1] S.V. Patanker, D.B. Spalding, A calculation procedure for the transient and steady state behaviour of shell and tube heat exchangers, Imperial College of Sci. Technol. Depart. Mech. Eng. (1972).

[2] C. Zhang, A.C.M. Sousa, J.E.S. Venart, Numerical simulation of different types of steam surface condensers, J. Energy Res. Technol. 113 (2) (1991) 63–70, https://doi.org/10.1115/1.2905788.

[3] C. Zhang, Y. Zhang, A quasi-three-dimensional approach to predict the performance of steam surface condensers, J. Energy Res. Technol. 115 (3) (1993) 213–220, https://doi.org/10.1115/1.2905996.

[4] C. Zhang, A. Bokil, A quasi-three-dimensional approach to simulate the two-phase fluid flow and heat transfer in condensers, Int. J. Heat Mass Transf. 40 (15) (1997) 3537–3546, https://doi.org/10.1016/S0017-9310(97)00014-8.

[5] H.G. Hu, C. Zhang, A modified k–ε turbulence model for the simulation of two-phase flow and heat transfer in condensers, Int. J. Heat Mass Transf. 50 (9) (2007) 1641–1648, https://doi.org/10.1016/j.ijheatmasstransfer.2006.10.031.

[6] H.G. Hu, C. Zhang, A new inundation correlation for the prediction of heat transfer in steam condensers, Numer. Heat Transf. A Appl. 54 (1) (2008) 34–46, https://doi.org/10.1080/10407780802024963.

[7] P. Mirzabeygi, C. Zhang, Three-dimensional numerical model for the two-phase flow and heat transfer in condensers, Int. J. Heat Mass Transf. 81 (2015) 618–637, https://doi.org/10.1016/j.ijheatmasstransfer.2014.10.015.

[8] P. Mirzabeygi, C. Zhang, Turbulence modeling for the two-phase flow and heat transfer in condensers, Int. J. Heat Mass Transf. 89 (2015) 229–241, https://doi.org/10.1016/j.ijheatmasstransfer.2015.05.044.

[9] J. Guo, et al., A novel approach for the optimal arrangement of tube bundles in a 1000-MW condenser, J. Zhejiang Uni-SCI. A 24 (12) (2023) 1140–1146, https://doi.org/10.1631/jzus.A2300183.

[10] H. Zeng, J.a. Meng, Z. Li, Numerical study of a power plant condenser tube arrangement, Appl. Therm. Eng. 40 (2012) 294–303, https://doi.org/10.1016/j.applthermaleng.2012.02.028.

[11] H. Zeng, J. Meng, Z. Li, Analysis of condenser shell side pressure drop based on the mechanical energy loss, Chin. Sci. Bull. 57 (36) (2012) 4718–4725, https://doi.org/10.1007/s11434-012-5558-4.

[12] A. Kumar, J.B. Joshi, A.K. Nayak, P.K. Vijayan, 3D CFD simulations of air cooled condenser-III: thermal–hydraulic characteristics and design optimization under forced convection conditions, Int. J. Heat Mass Transf. 93 (2016) 1227–1247, https://doi.org/10.1016/j.ijheatmasstransfer.2015.10.048.

[13] C. Abeykoon, Compact heat exchangers – design and optimization with CFD, Int. J. Heat Mass Transf. 146 (2020) 118766, https://doi.org/10.1016/j.ijheatmasstransfer.2019.118766.

[14] Habibullah, M. Atif, M.A. Khan, F.A. Awwad, E.A.A. Ismail, Thermal analysis and performance investigations of shell and tube heat exchanger using numerical simulations, Mod. Phys. Lett. B 38 (16) (2024) 2341015, https://doi.org/10.1142/S0217984923410154.

[15] M.M. Prieto, I.M. Suárez, E. Montanés, Analysis of the thermal performance of a church window steam condenser for different operational conditions using three models, Appl. Therm. Eng. 23 (2) (2003) 163–178, https://doi.org/10.1016/S1359-4311(02)00159-X.

[16] Y. Liao, et al., Study on three-dimensional numerical simulation of shell and tube heat exchanger of the surface ship under marine conditions, Nucl. Eng. Technol. 55 (4) (2023) 1233–1243, https://doi.org/10.1016/j.net.2022.12.020.

[17] W. Qiuwang, L. Hongxia, X. Gongnan, Z. Min, L. Laiqin, F. ZhenPing, Genetic algorithm optimization for primary surfaces recuperator of microturbine, J. Eng. Gas Turbines Power 129 (2) (2006) 436–442, https://doi.org/10.1115/1.2436550.

[18] V.K. Patel, R.V. Rao, Design optimization of shell-and-tube heat exchanger using particle swarm optimization technique, Appl. Therm. Eng. 30 (11) (2010) 1417–1425, https://doi.org/10.1016/j.applthermaleng.2010.03.001.

[19] S. Fettaka, J. Thibault, Y. Gupta, Design of shell-and-tube heat exchangers using multiobjective optimization, Int. J. Heat Mass Transf. 60 (2013) 343–354, https://doi.org/10.1016/j.ijheatmasstransfer.2012.12.047.

[20] A. Ghanei, E. Assareh, M. Biglari, A. Ghanbarzadeh, A.R. Noghrehabadi, Thermal-economic multi-objective optimization of shell and tube heat exchanger using particle swarm optimization (PSO), Heat Mass Transf. 50 (10) (2014) 1375–1384, https://doi.org/10.1007/s00231-014-1340-2.

[21] S. Sanaye, H. Hajabdollahi, Multi-objective optimization of shell and tube heat exchangers, Appl. Therm. Eng. 30 (14) (2010) 1937–1945, https://doi.org/10.1016/j.applthermaleng.2010.04.018.

[22] J. Guo, L. Cheng, M. Xu, Optimization design of shell-and-tube heat exchanger by entropy generation minimization and genetic algorithm, Appl. Therm. Eng. 29 (14) (2009) 2954–2960, https://doi.org/10.1016/j.applthermaleng.2009.03.011.

[23] P.D. Chaudhuri, U.M. Diwekar, J.S. Logsdon, An automated approach for the optimal design of heat exchangers, Ind. Eng. Chem. Res. 36 (9) (1997) 3685–3693, https://doi.org/10.1021/ie970010h.

[24] M. Fesanghary, E. Damangir, I. Soleimani, Design optimization of shell and tube heat exchangers using global sensitivity analysis and harmony search algorithm, Appl. Therm. Eng. 29 (5–6) (2009) 1026–1031, https://doi.org/10.1016/j.applthermaleng.2008.05.018.

[25] M.R. Daneshparvar, R. Beigzadeh, Multi-objective optimization of helical baffles in the shell-and-tube heat exchanger by computational fluid dynamics and genetic algorithm, Energy Rep. 8 (2022) 11064–11077, https://doi.org/10.1016/j.egyr.2022.08.249.

[26] W. Han, L. Tang, G. Xie, and Q. Wang, "Performance Comparison of Particle Swarm Optimization and Genetic Algorithm in Rolling Fin-Tube Heat Exchanger Optimization Design,". In: *ASME 2008 Heat Transfer Summer Conference collocated with the Fluids Engineering, Energy Sustainability, and 3rd Energy Nanotechnology Conferences*, 2008, vol. Heat Transfer: Volume 2, pp. 5-10, doi: 10.1115/ht2008-56213. [Online]. Available: DOI: 10.1115/HT2008-56213.

[27] R. Laskowski, A. Smyk, A. Rusowicz, A. Grzebielec, Determining the optimum inner diameter of condenser tubes based on thermodynamic objective functions and an economic analysis, Entropy 18 (12) (2016), https://doi.org/10.3390/e18120444.

[28] W.H. Saldanha, F.R.P. Arrieta, G.L. Soares, State-of-the-Art of research on optimization of shell and tube heat exchangers by methods of evolutionary computation, Arch. Comput. Meth. Eng. 28 (4) (2021) 2761–2783, https://doi.org/10.1007/s11831-020-09476-4.

[29] M. Serna, A. Jiménez, A compact formulation of the bell–delaware method for heat exchanger design and optimization, Chem. Eng. Res. Des. 83 (5) (2005) 539–550, https://doi.org/10.1205/cherd.03192.

[30] C. Wang, Z. Cui, H. Yu, K. Chen, J. Wang, Intelligent optimization design of shell and helically coiled tube heat exchanger based on genetic algorithm, Int. J. Heat Mass Transf. 159 (2020), https://doi.org/10.1016/j.ijheatmasstransfer.2020.120140.

[31] R. N. Al Sanea SA, Wilkinson TS., "Mathematical modelling of two-phase condenser flows,". In: *Proceedings of the BHRA 2nd International Conference on Multi-Phase Flow*, London, 1985, pp. 169-182.

[32] D. B. Rhodes and L. N. Carlucci, Predicted and measured velocity distribution in a model heat exchanger, Chalk River Nuclear Labs, Canada, 1984. [Online]. Available: http://inis.iaea.org/search/search.aspx?orig_q=RN:16042270.

[33] R. Clift, J. R. Grace, and M. E. Weber, Bubbles, drops, and particles, 2005.

[34] W. Wagner, et al., The IAPWS industrial formulation 1997 for the thermodynamic properties of water and steam, J. Eng. Gas Turbines Power 122 (1) (2000) 150–184, https://doi.org/10.1115/1.483186.

[35] F.W. Dittus, L.M.K. Boelter, Heat transfer in automobile radiators of the tubular type, Int. Commun. Heat Mass Transfer 12 (1) (1985) 3–22, https://doi.org/10.1016/0735-1933(85)90003-X.

[36] S. M. Ghiaasiaan, *Two-phase flow, boiling, and condensation: in conventional and miniature systems*. Cambridge University Press, 2017.

[37] L.D. Berman, Y.A. Tumanov, Investigation of heat transfer during condensation of moving vapor on a horizontal tube, Teplonergetika 10 (1962) 77–83.

[38] J. Kennedy and R. Eberhart, "Particle swarm optimization,". In: *Proceedings of ICNN'95 - International Conference on Neural Networks*, 27 Nov.-1 Dec. 1995 1995, vol. 4, pp. 1942-1948 vol.4, doi: 10.1109/ICNN.1995.488968.

[39] D. H. McAllister. *Unpublished work at NEI Parsons Limited*.

[40] A. S. Naviglio, M; Socrate, S; Stefani, A; Vigevano, L, "Distribution of non-condensable gases within the tube bundle of surface condensers," presented at the TEC 88-conference, Recent Advances in Heat Exchanger, Grenoble, France, 1988.

[41] F. Hecht. New development in FreeFem++. https://freefem.org/ (accessed 3-4, 20).